

Retina-Inspired Artificial Synapses with UV Modulated and Immediate Switchable Plasticity

Xuemei Zheng, Mengji Dong, Qi Li, Lu Wang, Yanli Liu, Xuan Di, Qilin Hua, Longfei Wang, Jianping Meng,* and Zhou Li*

As the most promising candidates for implementing in-sensor computing and lower power consumption, retina-inspired morphometric vision sensors must be able to perceive and discriminate images under various illumination conditions. However, integrating invisible ultraviolet (UV) light sensing and memory in a device is valuable for exploring advanced neuromorphic visual perception systems. Here, a retina-inspired artificial neuromorphic vision sensor based on GaN/BiFeO₃ heterojunction, which integrates sensing, memory, and processing functions, is presented. The device exhibits immediate switchable synapse plasticity-modulated ultra-weak UV illumination, including excitatory postsynaptic current (EPSC), paired-pulse facilitation (PPF), short-term and long-term plasticity (STP/LTP), and the learning-forgetting-relearning process. The maximum PPF index of the device is 200%, and the minimum excitation light intensity is 0.68 $\mu\text{W cm}^{-2}$. The phenomenon is attributed to the effective UV light modulation for negative polarization, ionization and de-ionization of the oxygen vacancies, further enhancing the persistent photoconductive (PPC) effect. In addition, the device successfully mimics human-like visual memory behavior by identifying the “BINN” letter pattern, which is extracted and visualized by invisible UV information from the learning-forgetting-relearning process. This work provides valuable insights into next-generation low-power and multi-functional photovoltaic artificial synapses.

solve structured problems, such as well-defined mathematical problems or processing precisely defined data sets.^[1,2] However, the progress of the internet of things and artificial intelligence requires high-performance and low-power consumption computers. For traditional computer architectures based on von Neumann architectures, the processor is separated from memory, resulting in the power consumption and computation time spent in reading data from memory to the extent that they cannot meet the demands of low-power and highly adaptive computing.^[3,4] The human brain is remarkably highly parallel and fault-tolerant because it performs distributed parallel computations with powerful storage space and high-speed computational capabilities in processing information from vision, hearing, taste, touch, and smell.^[5] Brain-like artificial neural networks (ANN) are considered one of the most promising information processing technologies for overcoming the von Neumann bottleneck.^[6] The human brain must process a great deal of visual information because over 80% comes from vision. The human brain can directly

process and store optical images, simplifying the circuit structure of neuromorphic vision systems and reducing power consumption during operation.^[7,8] Simulating the computational

1. Introduction

Traditional computers based on complementary metal oxide semiconductors (CMOS) and von Neumann architectures can

X. Zheng, M. Dong, Q. Li, L. Wang, Y. Liu, X. Di, Q. Hua, L. Wang, J. Meng, Z. Li
Beijing Institute of Nanoenergy and Nanosystems
Chinese Academy of Sciences
Beijing 101400, China
E-mail: mengjianping@binn.cas.cn; zli@binn.cas.cn

M. Dong, J. Meng, Z. Li
School of Nanoscience and Engineering
University of Chinese Academy of Sciences
Beijing 100049, China

Q. Li
College of Materials Science and Opto-Electronic Technology
University of Chinese Academy of Sciences
Beijing 100049, China

L. Wang
School of Physical Science and Technology
Guangxi University
Nanning 530004, China

Y. Liu, X. Di
School of Engineering and Technology
China University of Geosciences (Beijing)
Beijing 100083, China

Q. Hua
School of Integrated Circuits and Electronics
Beijing Institute of Technology
Beijing 100081, China

 The ORCID identification number(s) for the author(s) of this article can be found under <https://doi.org/10.1002/adfm.202420612>

DOI: 10.1002/adfm.202420612

and learning functions of synapses in the brain and designing synapse-like devices with synaptic behaviors and functions is a crucial step toward building brain-like computers. The realization of this step will advance the development of brain-like computers and bring breakthroughs in the fields of artificial intelligence and neuroscience.^[9]

Although much progress has been made in developing synapse-like devices, the speed of neural network computing is limited due to bandwidth-connection density trade-offs and interconnection issues between devices.^[8,10] Optoelectronic artificial synapses have been developed to overcome this obstacle. Compared with neuromorphic devices that have been extensively studied for electrical signal modulation, optoelectronic synaptic devices have remarkable properties, such as low crosstalk, high anti-interference, and low power consumption, which make them more suitable for ultra-high-speed computation.^[11,12] Moreover, optoelectronic artificial synaptic devices have the inherent advantage of processing visual information, which can achieve high-speed recognition and classification of image information.^[13] Various materials have been used to construct optoelectronic artificial synaptic devices, including 2D materials,^[14–16] metal oxides,^[17–19] silicon nanocrystals,^[20–22] organic materials,^[23,24] and metal halides.^[25–27] Optoelectronic artificial synaptic devices with different structures have been developed to simulate synaptic functions, including two-terminal and transistor-based three-terminal devices.^[28] Chen et al.^[29] simulated the hierarchical neural network of the insect's tiny visual system by preparing a double-layer MoS₂ transistor. By trapping carriers at the defect level to prevent the recombination of carriers, the current is continuously enhanced, and the device can accurately identify the movement of objects at different speeds. Jiang et al.^[23] developed an ultra-sensitive neuromorphic vision sensor based on organic phototransistors, which detects light intensity as low as 31 nW cm⁻². Due to the high selectivity of the device for ultraviolet light, the image can be denoised by filtering out red, green, and blue (RGB) noise, and the recognition accuracy of handwritten digits can reach up to 90%.

Compared with optoelectronic artificial synaptic devices with three-terminal structures, devices with two-terminal structures have been widely used in recent years due to the advantages of simple structure, low energy consumption, compatibility with high-density cross-array structures, and controllable photogenerated carrier transport and compounding processes.^[30] Among them, the photovoltaic effect, which is typical of the two-ended perpendicularly structured optoelectronic devices, implies that the devices can operate under light signals without the need to apply external bias, which is even more promising for the preparation of ultra-low-power optoelectronic neuro synaptic devices. Combining photosensitive and charge-trapping layers is an effective way to design a two-ended vertical structure, where the photosensitive layer endows the device with sensitive light responsiveness. The charge-trapping layer renders the device a persistent photoconductivity (PPC) effect, which can mimic various functions of biological synapses.^[31] Inspired by the photovoltaic effect, Huang et al. reported a self-powered optoelectronic synaptic device based on ITO/PCBM/MAPbI₃: Si NCs/Spiro-OMeTAD/Au vertical structure. The MAPbI₃/Si NCs hybrid film acts as the photosensitive layer of the synaptic device, and the heterojunction between Si NCs and MAPbI₃ can separate the pho-

togenerated electron-hole pairs. The photogenerated electrons and holes can move to ITO and Au, respectively, under the action of the built-in electric field so that the device can work at zero bias voltage. The work provides an effective strategy for realizing efficient neuromimetic computation with low energy consumption.^[32]

In our work, we successfully prepared a self-powered optoelectronic artificial synaptic device based on GaN/BiFeO₃ heterojunction. The device simulates multiple synaptic behaviors such as excitatory postsynaptic current (EPSC), paired-pulse facilitation (PPF), short-term plasticity (STP), long-term plasticity (LTP), and the learning-forgetting-relearning process. Additionally, we demonstrate that the optoelectronic artificial synapse exhibits immediate switchable plasticity under the modulation of UV light. Furthermore, the phenomenon demonstrates the effective UV light modulation for the negative polarization, ionization and de-ionization of the oxygen vacancies, further enhancing the persistent photoconductive (PPC) effect. The presented device has great potential in interactive neural networks and next-generation artificial intelligence, with applications in biological bionic vision, self-powered tunable functional devices, etc.

2. Results and Discussion

More than 80% of the external information is originated from our eyes. In the human visual system, the light emitted from external objects is collected by photoreceptor cells (cones and rods) on the retina and then converted into electrical signals.^[33] In response to external stimulation, the action potential releases neurotransmitters from presynaptic neurons transmit them to postsynaptic neurons and triggers excitatory postsynaptic currents (EPSC), which the brain can further interpret to construct physical images (**Figure 1a**). Inspired by the biological visual system, we fabricated a UV artificial neuromorphic vision sensor based on GaN/BiFeO₃ heterojunction, as shown in **Figure 1b**. GaN and BiFeO₃ film act as UV-sensitive materials during the optical synapse operation. As shown in **Figure S1** (Supporting Information), the stylus profiler-measured results indicate that the thickness value of the BiFeO₃ film is roughly 71.77 nm. **Figure 1c** shows the XRD patterns of BiFeO₃ films. As can be seen, diffraction peaks at 57.0° and 57.4° match well with the (122) and (300) crystal planes, respectively (PDF # 20–0169), which indicates the cubic lattice structure and high crystal quality of BiFeO₃ films. The intrinsic ferroelectric properties of the BiFeO₃ film are presented in **Figure 1d**. The ferroelectric domains exhibit distinct phase differences (red trace) and local hysteresis loops (blue trace). This indicates that the polarization state can be stably programmed by applying periodic forward and reverse voltage. Based on the transmittance curve provided for the BiFeO₃ film (**Figure S2**, Supporting Information), it indicates that the BiFeO₃ layer is capable of effectively absorbing UV light. In addition, the bandgap value of 2.65 eV for BiFeO₃ film is determined by absorbance spectra according to the Tauc equation (**Figure 1e**). XPS results confirm that the binding energies of the lattice oxygen and oxygen vacancies are 529.87 and 531.2 eV, with a percentage of 49.79% and 50.21%, respectively (**Figure 1f**), providing a direct proof of oxygen vacancies in BiFeO₃ films.

Based on the UV excitation and charge trap at the interface, the UV light-tunable synaptic plasticity is further investigated for the

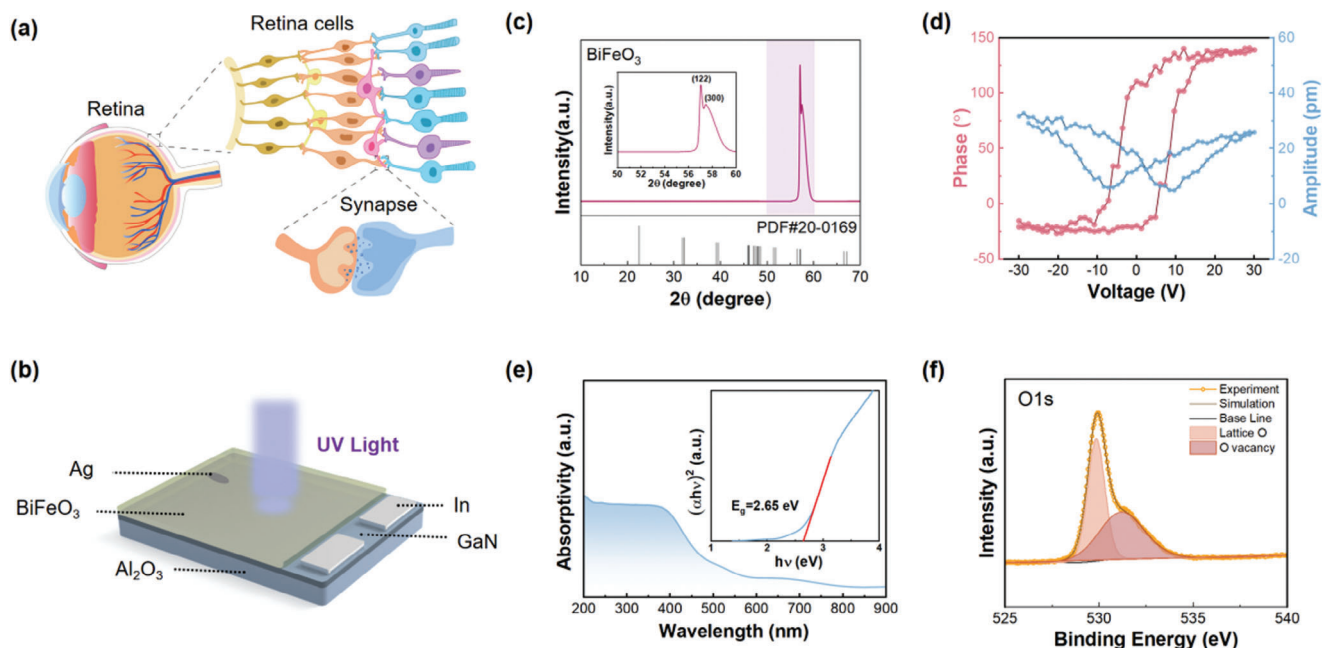


Figure 1. The GaN/BiFeO₃ heterojunction for UV artificial neuromorphic vision sensor. a) The schematic diagram of the artificial vision system includes a multilayer structure of the retina and its biological counterparts. b) Schematic illustration of the vertically artificial photoreceptor based on GaN/BiFeO₃ heterojunction. c) XRD patterns of BiFeO₃ films. d) Off-field PFM amplitude hysteresis loops (blue trace) and phase hysteresis (red trace) of BiFeO₃ film. e) UV-vis-NIR absorption curve of BiFeO₃ film. Inset: Tauc plot. f) The O 1s XPS spectra of BiFeO₃ films.

GaN/BiFeO₃ heterojunction under various UV illumination conditions. **Figure 2a** illustrates that the peak value of the EPSC could be enhanced by increasing the illumination intensity from 0.68 to 6.8 $\mu\text{W cm}^{-2}$. Similarly, the longer pulse duration can trigger stronger potentiation of EPSC under UV illumination intensity of 3.4 $\mu\text{W cm}^{-2}$ (Figure 2b). The same trend is also observed when the optical pulse frequency is increased from 1 to 5 Hz. Following the termination of the 1 Hz light pulse, the EPSC increased to 13 pA, inducing the short-term plasticity (STP) in artificial synapses. Furthermore, a higher optical frequency of 5 Hz excites the more photo-generated electron-hole pairs and achieves the enhanced EPSC of 59 pA. The longer decay time also displays the long-term plasticity (LTP) behavior. The EPSC and decay time can be effectively controlled by modulating the light pulse's intensity, width, and frequency to simulate the transition from STP to LTP. This can be mainly attributed to the persistent increase of photogenerated electrons under UV light irradiation.

Paired-pulse facilitation (PPF) represents a prevalent manifestation of STP, which pertains to the phenomenon whereby sustained presynaptic stimulation enhances postsynaptic signals. This process is critically important in the real-time decoding and recognition of visual or auditory information. Figure 2d shows a pair of UV pulses (325 nm, 3.4 $\mu\text{W cm}^{-2}$, pulse width = 2 s, interval time = 2 s) applied to the device. The EPSC generated by the second pulse (A_2) shows a significant increase compared to the EPSC elicited by the first pulse (A_1). The PPF index exhibits 200% at the interval time of 0.6 s and subsequently declines to $\approx 78\%$ when the interval exceeds 19 s. It demonstrates a rapid decline at the beginning, accompanied by an increase in the interval time. This phenomenon can be attributed to the incomplete collection of photogenerated electrons and holes by the electrodes follow-

ing the initial light pulse. Consequently, a greater accumulation of photogenerated carriers occurs following the subsequent light pulse. The PPF index is employed to examine synaptic behavior and can be defined by the following equation:^[34]

$$PPF = (A_2 - A_1) / A_1 \times 100\% \quad (1)$$

where A_1 and A_2 denote the currents excited by the first and second pulses, respectively. Figure 2e illustrates that the PPF index exhibited a progressive decline as the interval time increased from 0.6 to 19 s. This decay trend can be accurately modeled by the following double-exponential function, which closely resembles the observed behavior of biological synapses.^[35]

$$PPF \text{ Index} = C_1 \times \exp\left(-\frac{\Delta t}{\tau_1}\right) + C_2 \times \exp\left(-\frac{\Delta t}{\tau_2}\right) \quad (2)$$

where Δt represents the time interval between optical pulses, C_1 and C_2 correspond to the initial facilitation magnitudes, and τ_1 and τ_2 represent the characteristic relaxation time for rapid and slow decay phases. As a result, the values of C_1 , C_2 , τ_1 , and τ_2 are 100.77, 134.87, 1.52, and 35.05 s, respectively. It can be seen that τ_1 is an order of magnitude smaller than τ_2 , similar to the decay kinetics observed in biological synapses.

Furthermore, the repeatable plasticity of biological synapses enables the human brain to align with the Ebbinghaus forgetting curve, which refers to the rapid decline in memory retention over time, and the relearning process takes less time to remember the same information than the initial learning process. The device is stimulated with 20 consecutive light pulses to mimic "learning experience" behavior (Figure 2f). The current increases from 3

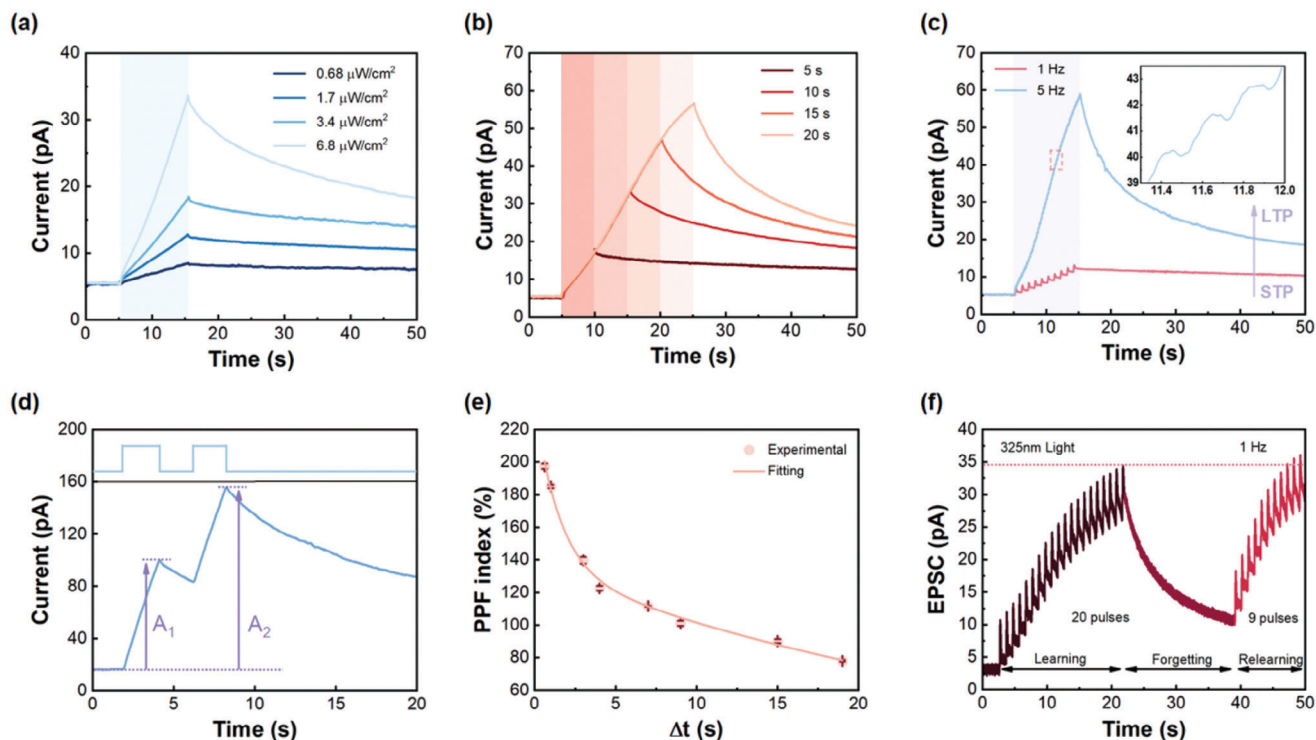


Figure 2. Synaptic plasticity of GaN/BiFeO₃ artificial synapse under various UV illumination conditions. a) Various UV illumination (325 nm) intensities. b) Various pulse widths under UV illumination intensity of 3.4 μW cm⁻². c) Dependence of the decay characteristics under various frequencies of UV illumination. d) Paired-pulse facilitation (PPF) behavior under UV illumination stimulations with an interval of 2 s. e) Dependence of the PPF index on the different interval times (Δt) between pairs of pulses. f) UV light-induced learning-forgetting-relearning process.

to 34.4 pA in the initial learning process, with the light continuously simulated. Once the light is switched off, the current declines rapidly, corresponding to the forgetting process after learning. Light pulses are reapplied to the device to enhance memory strength and imitate the relearning process. It is observed that only nine pulses are required to restore the previous learning level, which is a significant reduction compared to the initial learning period. This behavior is analogous to that observed in humans, demonstrating the potential of the GaN/BiFeO₃ heterojunction in emulating the “learning-forgetting-relearning” function. As depicted in Figure S3 (Supporting Information), it is

observed that there is no photoresponse under illumination of 405 nm with a power density of 1.92 mW cm⁻², attributing to the thin thickness of the BiFeO₃ film and low photon energy of blue light. Our device exhibits the selectivity for UV light and can operate at a low power density (0.68 μW cm⁻²) compared to other devices (Table S1, Supporting Information).

To clarify the working mechanism of GaN/BiFeO₃ heterojunction, the band structure and carrier transport process are depicted in Figure 3. GaN/BiFeO₃ heterojunction can form a typical type II band structure according to their structure of energy band level (Figure 3a). As illustrated in Figure S4 (Supporting Information),

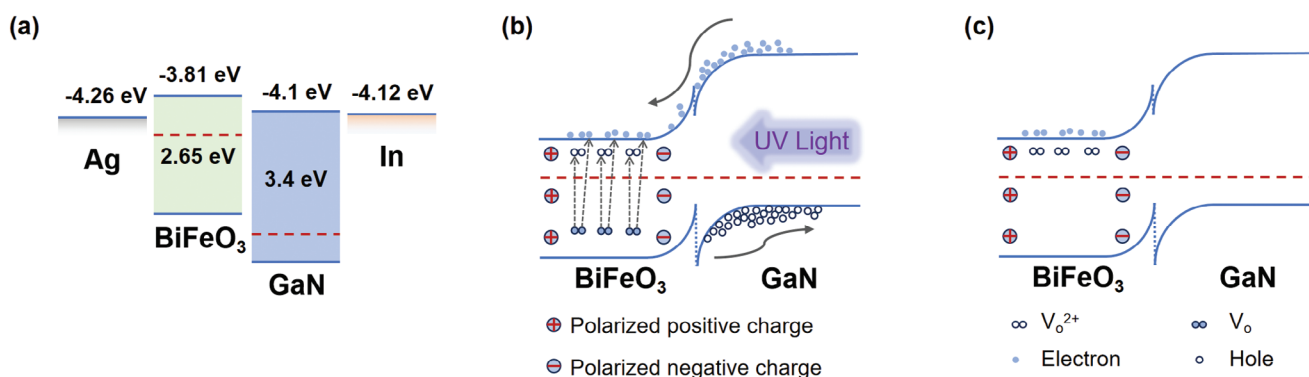


Figure 3. The working mechanism of the GaN/BiFeO₃ heterojunction. a) Schematic diagram of the energy band structure of the GaN/BiFeO₃ heterojunction. b) GaN/BiFeO₃ heterojunction under UV light illumination. c) After removing UV light illumination.

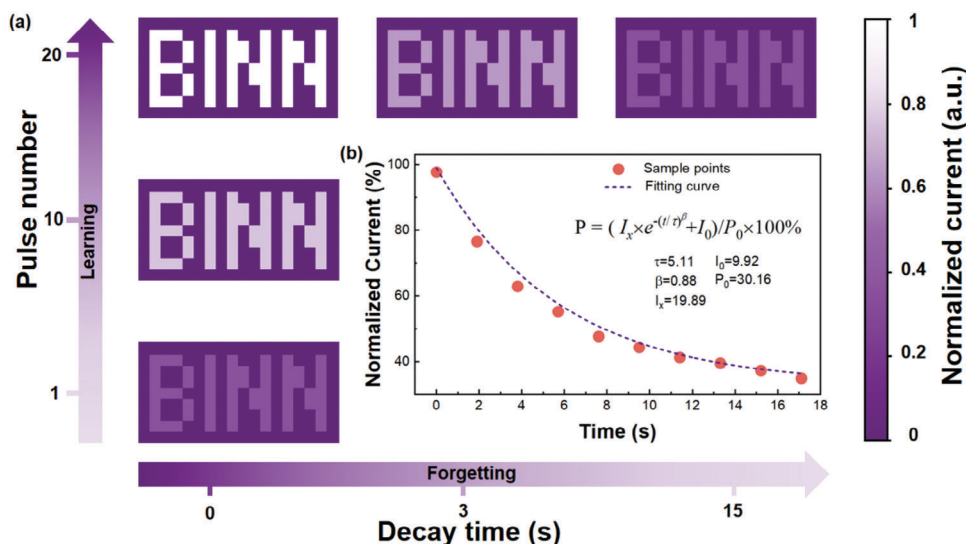


Figure 4. Visual memory emulation of the GaN/BiFeO₃ heterojunction based-UV artificial neuromorphic sensor. a) The variation in normalized EPSC mapping images with a “BINN” letter pattern with decay time (horizontal axis) under increasing UV light pulse numbers (vertical axis). b) The image-forgetting process aligns with the Ebbinghaus forgetting curve.

the linear I – V curve demonstrates the Ohmic contact is formed between GaN and In, benefiting the collection of carriers. The built-in potential created by the GaN/BiFeO₃ heterojunction not only facilitates the separation and transport of photogenerated carriers but also plays an essential role in synaptic plasticity. Under UV light illumination, photogenerated electron-hole pairs are promptly separated by built-in potential and collected by the Ag and In electrodes. Meanwhile, the neutral oxygen vacancies (Vo) in the BiFeO₃ film, a large number of electrically are present. Under the action of UV light, these Vo convert to the ionized oxygen vacancy (Vo²⁺) and electrons (Figure 3b). This ionization and deionization process of oxygen vacancies effectively traps and releases carriers, which is a key factor in enhancing the persistent photoconductive (PPC) effect and is also closely related to the modulation of synaptic plasticity. The trapped carriers can influence the synaptic weight and the time-dependent behavior of the synapse, similar to the learning and forgetting processes in biological synapses. After the light is removed, Vo²⁺ and electrons do not immediately recombine due to the presence of energy barriers (Figure 3c). In addition, the negative polarization charge raises the height of the barrier at the conduction band, resulting in some electrons trapped at the barrier and unable to recombine with holes quickly. This phenomenon further enhances the PPC effect and endows the device with the capacity to imitate the long-term memory behavior of biological synapses.

In the human visual system, repeatable stimulation of retinal cells by an optical image leads to an increase in synaptic weight among the visual nerves. The more detailed and precise an image is, the less likely it is to be forgotten. To emulate the visual memory imaging effects, we employ a visualization approach to simulate the learning-forgetting-relearning process based on the modulation of synaptic plasticity. The “BINN” letter pattern is used to investigate the visual memory features of the GaN/BiFeO₃ heterojunction based-UV artificial neuromorphic vision sensor (Figure 4). As the number of light pulses increases to 1 or even 20, the light-induced normalized current increases, allowing the

achievement of a high-contrast mapped letter “BINN.” Furthermore, the image remained discernible even after the decay time of 15 s (Figure 4a). The results demonstrate that light information can be perceived and memorized quickly, indicating its potential for emulating human visual memory functions.

To further analyze the behaviors of the learning-forgetting-relearning, the Ebbinghaus forgetting curve is aligned with Equation (2):^[36]

$$P = (I_x e^{-(t/\tau)^\beta} + I_0) / P_0 \times 100\% \quad (3)$$

where P is the possibility of recall, I_x is the pre-exponential factor, t is time, τ is the specific relaxation time, β is the exponent that ranges from 0 to 1, and I_0 is the stable current after EPSC decays, P_0 is the initial value when there is no forgetting. As shown in Figure 4b, the forgetting process of the image aligns closely with the Ebbinghaus forgetting curve, with τ and β values of 5.11 s and 0.88, respectively. This exemplifies the GaN/BiFeO₃ heterojunction-based-UV artificial neuromorphic vision sensor in brain-like learning and memory capabilities, thereby highlighting its immense potential in advancing the human visual system.

3. Conclusion

In summary, we present a UV light-sensitive and polarization-dependent artificial synaptic device based on GaN/BiFeO₃ heterojunction. The device features immediate switchable plasticity under the modulation of ultra-weak UV light, including EPSC, PPF, STP/LTP, and the learning-forgetting-relearning process. The maximum PPF index of the device is 200%, and the minimum excitation light intensity is 0.68 $\mu\text{W cm}^{-2}$. Additionally, the phenomenon demonstrates that the large number of oxygen vacancies present in BiFeO₃ thin films can undergo ionization and deionization. The local ferroelectric field generated by

BiFeO₃ thin films can enhance the energy barrier at the conduction band, resulting in the effect of photoelectron traps. The combined effect of these two factors resulted in the device exhibiting a persistent photoconductivity (PPC) effect, enabling the device to simulate synaptic performance successfully. Moreover, the visual memory imaging effects mimic human-like visual memory behavior by identifying the “BINN” letter pattern, which is extracted and visualized by invisible UV information from the learning-forgetting-relearning process. The presented device shows great prospects in constructing next-generation artificial intelligence neuromorphic vision systems, multi-functional photovoltaic artificial synapses, etc.

4. Experimental Section

Fabrication of GaN/BiFeO₃ Heterojunction Devices: First, the p-type GaN of sapphire substrate was cut by laser technology and then cleaned by ultrasonication for 15 min with acetone, ethanol, and deionized water, respectively. Second, the BiFeO₃ layer was obtained on a pre-cleaned GaN substrate by radio frequency (RF) magnetron sputtering (Denton, Discovery 635, USA) for 90 min using a BiFeO₃ target in a high vacuum (vacuum degree: 3.1×10^{-4} Torr). During sputtering, the RF power was 100 W in a pure argon ambient at 40 sccm. Then, Ag and Indium as the top and bottom electrodes were deposited on the BiFeO₃ film and GaN substrate surface, respectively. Finally, a polarization field with the high voltage power source (ENTAI, ET2673A, China) was applied for 30 min to polarize the BiFeO₃ films before the measurement. All the measurements were performed in an ambient atmosphere and at room temperature.

Material Characterization: The XRD pattern was obtained by an X-ray diffractometer (PANalytical X'Pert) using Cu K α radiation ($\lambda = 1.54 \text{ \AA}$). The ferroelectricity characteristics of BiFeO₃ films were recorded in tapping mode utilizing the Piezoresponse force microscope (PFM, Asylum Research, MFP-3D-SA, USA). The absorbance and transmittance curves of samples were characterized by a UV-vis-NIR spectrometer (Shimadzu UV 3600) at room temperature. The concentration of oxygen vacancies (Vo) in the BiFeO₃ films was determined by X-ray photoelectron spectroscopy (XPS, Thermo Fisher ESCALAB). A profilometer (DektakXT) was used to measure the thickness of the BiFeO₃ film.

Device Characterization: The synaptic functionalities were characterized by a laboratory-built photoelectric test system, including a laser-confocal microscope Raman spectrometer system (LabRAM HR Evolution, Horiba), a pulse generator (EDINBURGH PHOTONICS, μ F2), LeCroy oscilloscope, and a Keithley 6517B source meter. The monochromatic 325 nm laser was used to apply persistent light on top of the device. A continuously variable attenuator modulated the light power density in the Raman System. The corresponding power intensity of the light pulse was measured by digital optical power meters (THORLBS PM100D, Dachau, Germany). The frequency of optical spikes was controlled by a pulse generator, which was utilized to generate constant or periodical light illumination. A LeCroy oscilloscope and a Keithley 6517B source meter measured and recorded the electrical signal.

Supporting Information

Supporting Information is available from the Wiley Online Library or from the author.

Acknowledgements

X.Z. and M.D. contributed equally to this work. The authors are thankful for the support provided by the National Natural Science Foundation of China (52472174, T2125003), the National Key R & D Project from the Minister

of Science and Technology (2023YFB3208101), the Youth Innovation Promotion Association CAS (2023175), and the Natural Science Foundation of Beijing Municipality (Z240022).

Conflict of Interest

The authors declare no conflict of interest.

Data Availability Statement

Research data are not shared.

Keywords

artificial neuromorphic vision sensor, persistent photoconductive (PPC) effect, synapse plasticity, UV light modulation, visual memory imaging effects

Received: October 28, 2024

Revised: January 24, 2025

Published online:

- [1] J. Von Neumann, *IEEE Ann. Hist. Comput* **1993**, *15*, 27.
- [2] D. Kuzum, S. Yu, H. P. Wong, *Nanotechnology* **2013**, *24*, 382001.
- [3] Z. Hao, H. Wang, S. Jiang, J. Qian, X. Xu, Y. Li, M. Pei, B. Zhang, J. Guo, H. Zhao, *Adv. Sci* **2022**, *9*, 2103494.
- [4] T. Y. Wang, J. L. Meng, Z. Y. He, L. Chen, H. Zhu, Q. Q. Sun, S. J. Ding, P. Zhou, D. W. Zhang, *Adv. Sci* **2020**, *7*, 1903480.
- [5] J. T. Yang, C. Ge, J. Y. Du, H. Y. Huang, M. He, C. Wang, H. B. Lu, G. Z. Yang, K. J. Jin, *Adv. Mater.* **2018**, *30*, 1801548.
- [6] W. Huang, X. Xia, C. Zhu, P. Steichen, W. Quan, W. Mao, J. Yang, L. Chu, X. A. Li, *Nanomicro Lett.* **2021**, *13*, 1.
- [7] Y. Hu, M. Dai, W. Feng, X. Zhang, F. Gao, S. Zhang, B. Tan, J. Zhang, Y. Shuai, Y. Fu, *Adv. Mater.* **2021**, *33*, 2104960.
- [8] F. Zhou, Z. Zhou, J. Chen, T. H. Choy, J. Wang, N. Zhang, Z. Lin, S. Yu, J. Kang, H.-S. P. Wong, *Nat. Nanotechnol.* **2019**, *14*, 776.
- [9] Y. Li, G. Shen, *Cell Rep. Phys. Sci.* **2022**, *3*, 101037.
- [10] M. M. Islam, A. Krishnaprasad, D. Dev, R. Martinez-Martinez, V. Okonkwo, B. Wu, S. S. Han, T.-S. Bae, H.-S. Chung, J. Tourma, *ACS Nano* **2022**, *16*, 10188.
- [11] Z.-D. Luo, X. Xia, M.-M. Yang, N. R. Wilson, A. Gruverman, M. Alexe, *ACS Nano* **2019**, *14*, 746.
- [12] M. Kumar, J. Lim, S. Kim, H. Seo, *ACS Nano* **2020**, *14*, 14108.
- [13] L. Mennel, J. Symonowicz, S. Wachter, D. K. Polyushkin, A. J. Molina-Mendoza, T. Mueller, *Nature* **2020**, *579*, 62.
- [14] J. Jiang, W. Hu, D. Xie, J. Yang, J. He, Y. Gao, Q. Wan, *Nanoscale* **2019**, *11*, 1360.
- [15] T. Ahmed, S. Kuriakose, E. L. Mayes, R. Ramanathan, V. Bansal, M. Bhaskaran, S. Sriram, S. Walia, *Small* **2019**, *15*, 1900966.
- [16] T. Zhao, C. Zhao, W. Xu, Y. Liu, H. Gao, I. Z. Mitrovic, E. G. Lim, L. Yang, C. Z. Zhao, *Adv. Funct. Mater.* **2021**, *31*, 2106000.
- [17] J. Sun, S. Oh, Y. Choi, S. Seo, M. J. Oh, M. Lee, W. B. Lee, P. J. Yoo, J. H. Cho, J. H. Park, *Adv. Funct. Mater.* **2018**, *28*, 1804397.
- [18] M. K. Kim, J. S. Lee, *Adv. Mater.* **2020**, *32*, 1907826.
- [19] S. Hong, H. Cho, B. H. Kang, K. Park, D. Akinwande, H. J. Kim, S. Kim, *ACS Nano* **2021**, *15*, 15362.
- [20] Y. Zhu, W. Huang, Y. He, L. Yin, Y. Zhang, D. Yang, X. Pi, *Research* **2020**, 7538450.
- [21] L. Yin, C. Han, Q. Zhang, Z. Ni, S. Zhao, K. Wang, D. Li, M. Xu, H. Wu, X. Pi, *Nano Energy* **2019**, *63*, 103859.

- [22] S. Zhao, Z. Ni, H. Tan, Y. Wang, H. Jin, T. Nie, M. Xu, X. Pi, D. Yang, *Nano Energy* **2018**, *54*, 383.
- [23] T. Jiang, Y. Wang, Y. Zheng, L. Wang, X. He, L. Li, Y. Deng, H. Dong, H. Tian, Y. Geng, L. Xie, Y. Lei, H. Ling, D. Ji, W. Hu, *Nat. Commun.* **2023**, *14*, 2281.
- [24] C. Qian, S. Oh, Y. Choi, J.-H. Kim, J. Sun, H. Huang, J. Yang, Y. Gao, J.-H. Park, J. H. Cho, *Nano Energy* **2019**, *66*, 104095.
- [25] B. Pradhan, S. Das, J. Li, F. Chowdhury, J. Cherusseri, D. Pandey, D. Dev, A. Krishnaprasad, E. Barrios, A. Towers, *Sci. Adv.* **2020**, *6*, eaay5225.
- [26] S. Ham, S. Choi, H. Cho, S. I. Na, G. Wang, *Adv. Funct. Mater.* **2019**, *29*, 1806646.
- [27] Q.-B. Zhu, B. Li, D.-D. Yang, C. Liu, S. Feng, M.-L. Chen, Y. Sun, Y.-N. Tian, X. Su, X.-M. Wang, *Nat. Commun.* **2021**, *12*, 1798.
- [28] D. Hao, Z. Yang, J. Huang, F. Shan, *Adv. Funct. Mater.* **2023**, *33*, 2211467.
- [29] J. Chen, Z. Zhou, B. J. Kim, Y. Zhou, Z. Wang, T. Wan, J. Yan, J. Kang, J.-H. Ahn, Y. Chai, *Nat. Nanotechnol.* **2023**, *18*, 882.
- [30] J. Gong, H. Yu, X. Zhou, H. Wei, M. Ma, H. Han, S. Zhang, Y. Ni, Y. Li, W. Xu, *Adv. Funct. Mater.* **2020**, *30*, 2005413.
- [31] F. Ma, Y. Zhu, Z. Xu, Y. Liu, X. Zheng, S. Ju, Q. Li, Z. Ni, H. Hu, Y. Chai, *Adv. Funct. Mater.* **2020**, *30*, 1908901.
- [32] W. Huang, P. Hang, Y. Wang, K. Wang, S. Han, Z. Chen, W. Peng, Y. Zhu, M. Xu, Y. Zhang, Y. Fang, X. Yu, D. Yang, X. Pi, *Nano Energy* **2020**, *73*, 104790.
- [33] Y. Gong, P. Xie, X. Xing, Z. Lv, T. Xie, S. Zhu, H. H. Hsu, Y. Zhou, S. T. Han, *Adv. Funct. Mater.* **2023**, *33*, 2303539.
- [34] S. Ge, F. Huang, J. He, Z. Xu, Z. Sun, X. Han, C. Wang, L. B. Huang, C. Pan, *Adv. Opt. Mater.* **2022**, *10*, 2200409.
- [35] Q. Liu, L. Yin, C. Zhao, J. Wang, Z. Wu, H. Lei, Y. Liu, B. Tian, Z. Zhang, Z. Zhao, *Nano Energy* **2022**, *102*, 107686.
- [36] Y. Chen, Y. Li, S. Niu, X. Yang, W. Dou, C. Shan, G. Shen, *Adv. Funct. Mater.* **2024**, *34*, 2315383.